Multimetallic Alloy Nanotubes with Nanoporous Framework

Bu-Seo Choi,[†] Young Wook Lee,[†] Shin Wook Kang,[†] Jong Wook Hong,[†] Jung Kim,[‡] Inkyu Park,[‡,*] and Sang Woo Han[†,*]

[†]Department of Chemistry and KI for the NanoCentury and [‡]Department of Mechanical Engineering and KI for the NanoCentury, KAIST, Daejeon 305-701, Korea

ABSTRACT One-dimensional nanotubes (NTs) that consist of multiple metallic components are promising platforms for potential applications, whereas only a few synthetic methods of multimetallic NTs have been reported to date. In the present work, we developed a general synthesis route for the production of uniform multicomponent one-dimensional tubular nanostructures with various combinations of Pt, Pd, and Ag by using ZnO nanowires (NWs) as sacrificial templates. The ZnO NWs serve not only as physical templates but also as nucleation sites for the reduction of metal precursors, and thereby several metal precursors could be reduced simultaneously to produce multimetallic NTs. By using this approach, Pt—Pd, Pt—Ag, and Pd—Ag binary alloy NTs, and even Pt—Pd—Ag ternary alloy NTs could be successfully prepared. The prepared Pt—Pd binary alloy NTs exhibited improved electrocatalytic activity and stability toward ethanol oxidation due to their characteristic tubular morphology with well-interconnected nanoporous framework and synergism between two constituent metals. Furthermore, our approach can facilitate the fabrication of patterned multimetallic NT arrays on solid and flexible substrates with strong mechanical robustness. The present templating method does not require any extra steps to remove templates or additional surfactants which are often required to control the shape of nanostructures. This strategy offers a convenient, versatile, low-cost, and highly valuable approach to the fabrication of multimetallic nanostructures with various components and compositions.

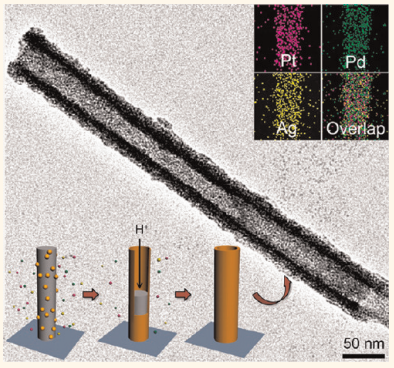

KEYWORDS: alloys · electrocatalysis · nanoporous frameworks · nanotubes · ZnO nanowires

Multimetallic alloy nanostructures have shown pronounced electronic, catalytic, and optical properties over individual constituent metals *via* synergism between the components, thus enabling their use as efficient electrocatalysts,[1,2] chemical catalysts,[3] and surface-enhanced Raman scattering (SERS) substrates.[4,5] Furthermore, the formation of alloyed structures by introducing other metals has been adopted as a strategy to overcome the drawbacks of targeted metals. For instance, cost-issues can be addressed by adding economical metals[6,7] and stability can be enhanced by the incorporation of robust metals.[8] Because the properties of metal nanostructures highly depend on their shape as well as size and composition,[9−11] controlling the morphology of multimetallic alloy nanostructures is an important issue in terms of optimizing their properties. However, manipulating the shape of alloy nanostructures is not a straightforward task due to the difficulties involved in controlling the nucleation and growth of nanostructures in the presence of various metal precursors with different reduction kinetics.

Among myriad types of shaped-nanostructures, one-dimensional (1D) tubular structures are particularly attractive due to their unique morphology and high surface to volume ratio, which can promote their catalytic or sensing properties.[12,13] Accordingly, nanotubes (NTs) that consist of multiple metallic components are promising platforms for potential applications, although only a few synthetic methods of 1D multimetallic NTs have been reported to date. Anodized aluminum oxide (AAO) has been used as a physical template to generate multimetallic NTs by electro-deposition.[14] However, an additional step for removing the templates is required. Besides, galvanic replacement reactions using metal nanowires (NWs) as sacrificial templates were used to yield metallic NTs.[15,16] However, application of this approach is limited to metals that have sufficiently higher reduction potential values than that of the metal composing the sacrificial NWs.

In the present work, we developed a facile hydrothermal method to prepare multimetallic NTs with various combinations of noble metals such as Pt, Pd, and Ag by using ZnO NWs as sacrificial templates, based on our previous studies.[17,18] The ZnO NWs serve not only as physical templates but also as nucleation sites for the reduction of metal precursors, and thereby several metal precursors could be reduced simultaneously to produce multimetallic NTs. By using this

* Address correspondence to sangwoohan@kaist.ac.kr, inkyu@kaist.ac.kr.

Received for review April 16, 2012 and accepted May 21, 2012.

Published online May 21, 2012
10.1021/nn301660x

approach, Pt–Pd, Pt–Ag, and Pd–Ag binary alloy NTs, and even Pt–Pd–Ag ternary alloy NTs could be successfully prepared. Since the ZnO NW templates were dissolved during the reduction of the metal precursors, there is no need to eliminate the templates to construct hollow interiors. This method provides a simple, economical, and general approach for the fabrication of multimetallic alloy NTs regardless of the different reduction kinetics of various metal precursors.

RESULTS AND DISCUSSION

In the first step, ZnO NW arrays grown on Si wafers were prepared for templates (see Methods section). The average length and diameter of the ZnO NWs were about 1.5 μm and 30 nm, respectively (Figure S1 in the Supporting Information (SI)). To produce NTs, the ZnO NWs were immersed into an aqueous solution containing metal precursors and a small amount of sodium citrate, and the reaction mixture was then heated at ~95 °C for about 1 h in a conventional drying oven. Figure 1 panels a, d, and g show typical scanning electron microscopy (SEM) images of Pt–Pd, Pt–Ag, and Pd–Ag bimetallic NTs, respectively, indicating the uniform formation of 1D tubular nanostructures with open tips. Pt–Pd, Pt–Ag, and Pd–Ag bimetallic NTs were prepared by using K_2PtCl_4/K_2PdCl_4 (1:1), $K_2PtCl_4/AgNO_3$ (2:1), and $K_2PdCl_4/AgNO_3$ (2:1) mixtures as metal precursors, respectively. The hollow interiors of NTs were more clearly evidenced by transmission electron microscopy (TEM) measurements (Figure 1b,e,h). The average outer diameters and wall thicknesses of bimetallic NTs are, respectively, 70 and 17 nm for Pt–Pd NTs (Figure 1b), 59 and 12 nm for Pt–Ag NTs (Figure 1e), and 83 and 19 nm for Pd–Ag NTs (Figure 1h). TEM images also reveal rough outer surfaces of the NTs. This can be attributed to the aggregation of 2–3 nm sized nanocrystalline segments (see the high-magnification TEM images shown in Figure S2 in SI). These three-dimensionally interconnected nanoparticles result in the formation of porous walls of NTs. The resultant nanoporous framework can significantly increase the surface area and density of active surface sites, and can also enhance mass transport.[19–21] As such, it is anticipated that the synthesized NTs may show highly efficient catalytic functions.

High-resolution TEM (HRTEM) images further reveal that the nanoparticles forming the three-dimensional networks have random orientations and their lattice fringes are well-correlated to representative {111} crystallographic planes (insets of Figure 1b,e,h). The *d*-spacings for adjacent lattice planes are 2.24, 2.29, and 2.29 Å for Pt–Pd, Pt–Ag, and Pd–Ag NTs, respectively, corresponding to the (111) planes of face-centered cubic (*fcc*) Pt–Pd, Pt–Ag, and Pd–Ag alloys (*d*-spacings for the (111) planes of pure Pt, Pd, and Ag are 2.25, 2.24, and 2.36 Å, respectively). These characteristic *d*-spacing values suggest that the nanoparticles are an alloy of two respective metal

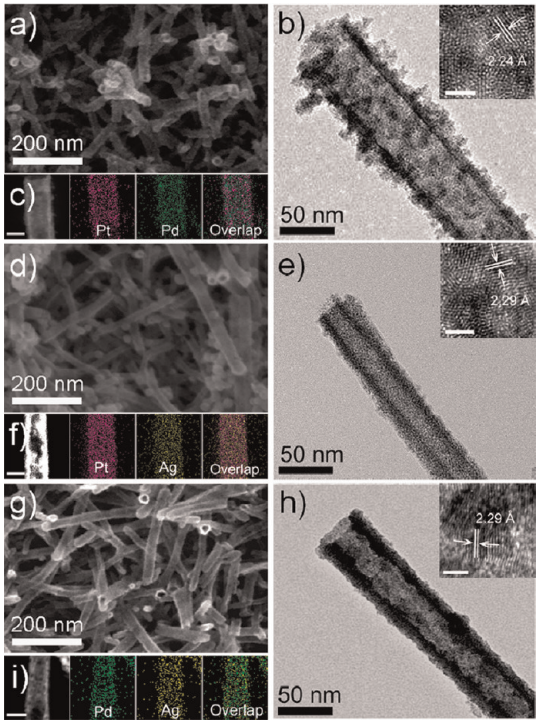

Figure 1. (a) SEM, (b) TEM, and (c) HAADF-STEM-EDS mapping images of the Pt–Pd NTs. HRTEM image is shown in the inset of panel b. (d) SEM, (e) TEM, and (f) HAADF-STEM-EDS mapping images of the Pt–Ag NTs. HRTEM image is shown in the inset of panel e. (g) SEM, (h) TEM, and (i) HAADF-STEM-EDS mapping images of the Pd–Ag NTs. HRTEM image is shown in the inset of panel h. The scale bars in insets of panels b, e, and h indicate 2 nm. The scale bars in panels c, f, and i indicate 50 nm.

components. To confirm the compositional distribution of each bimetallic NT, elemental mapping analyses were performed by high-angle annular dark-field scanning TEM-energy-dispersive X-ray spectroscopy (HAADF-STEM-EDS) (Figure 1c, f, i). The observed uniform distributions with full overlap of the two respective metal elements throughout the tubular morphology unambiguously demonstrate that the prepared NTs are alloys of Pt–Pd (Figure 1c), Pt–Ag (Figure 1f), and Pd–Ag (Figure 1i). The compositional line profiles measured through the cross-section of each bimetallic NT by HAADF-STEM-EDS further support the formation of homogeneous alloys (Figure S3 in SI). Moreover, the lower density of both metals at the center of NTs and the higher density at the edges of NTs in the compositional line profiles are evidence of the hollow structures of NTs. The actual Pt:Pd, Pt:Ag, and Pd:Ag molar ratios for Pt–Pd, Pt–Ag, and Pd–Ag NTs were estimated to be 31:69, 74:26, and 57:43, respectively, by using an inductively coupled plasma-atomic emission spectrometer (ICP–AES).

Interestingly, the present method could be extended to the fabrication of trimetallic NTs. Pt–Pd–Ag ternary alloy NTs with uniform size were generated by using a $K_2PtCl_4/K_2PdCl_4/AgNO_3$ mixture as a metal precursor. SEM (Figure 2a) and TEM (Figure 2b) images of the as-prepared Pt–Pd–Ag trimetallic NTs with a

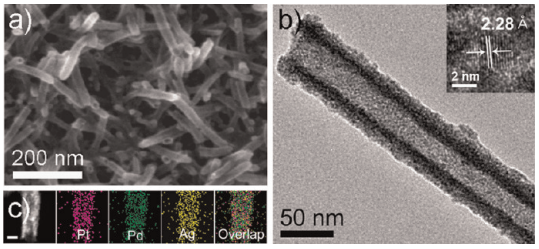

Figure 2. (a) SEM, (b) TEM, and (c) HAADF-STEM-EDS mapping images of the Pt−Pd−Ag NTs. HRTEM image is shown in the inset of panel b. The scale bar in panel c indicates 50 nm.

1:1:1 $K_2PtCl_4/K_2PdCl_4/AgNO_3$ mixture show well-defined tubular nanostructures. The average outer diameter and wall thickness of the trimetallic NTs are 61 and 22 nm, respectively. A high-magnification TEM image of NTs revealed the formation of a porous wall consisting of 2−3 nm sized nanoparticles as in the case of binary alloy NTs (Figure S2d in SI). The *d*-spacing of 2.28 Å for adjacent lattice planes measured by HRTEM corresponds to the intermediate value of the (111) planes of pure *fcc* Pt, Pd, and Ag (inset of Figure 2b). In addition, the elemental mapping (Figure 2c) and compositional line profiles (Figure S3d in SI) on a single NT measured by HAADF-STEM-EDS clearly indicate that the synthesized NTs are an alloy of Pt, Pd, and Ag. The molar percentage of each metallic component in the prepared Pt−Pd−Ag NTs measured by an ICP-AES analysis was 52.5, 27.1, and 20.4% for Pt, Pd, and Ag, respectively.

The X-ray diffraction (XRD) patterns of the Pt−Pd, Pt−Ag, Pd−Ag, and Pt−Pd−Ag NTs show distinct diffraction peaks from the reflections of the *fcc* structure of the metal (Figure S4 in SI), revealing the crystalline nature of the prepared NTs. The peaks from ZnO could not be identified, which also reflects the effective removal of ZnO NW templates. In particular, it is noticeable that the 2θ values of the Pt−Ag, Pd−Ag, and Pt−Pd−Ag alloy NTs lie between those of pure Ag and Pt/Pd, indicating the formation of single-phase alloy NTs.

To elucidate the formation mechanism of multimetallic NTs, temporal changes in the morphology and composition of Pt−Pd−Ag trimetallic NTs were investigated as a representative example. The TEM images obtained at different reaction times show both the formation of tubular walls on the ZnO NW templates and the simultaneous elimination of the templates (Figure 3a−e). The HRTEM image of a pristine ZnO NW shown in the inset of Figure 3a illustrates a *d*-spacing of 2.5 Å between adjacent lattice planes along the longitudinal axis, which coincides with that of the (002) lattice planes of hexagonal wurtzite ZnO.[22−24] This confirms that single crystalline ZnO NWs were grown along the [001] *c*-axis direction. At the initial stage of the reaction, a small number of nanoparticles grew on the

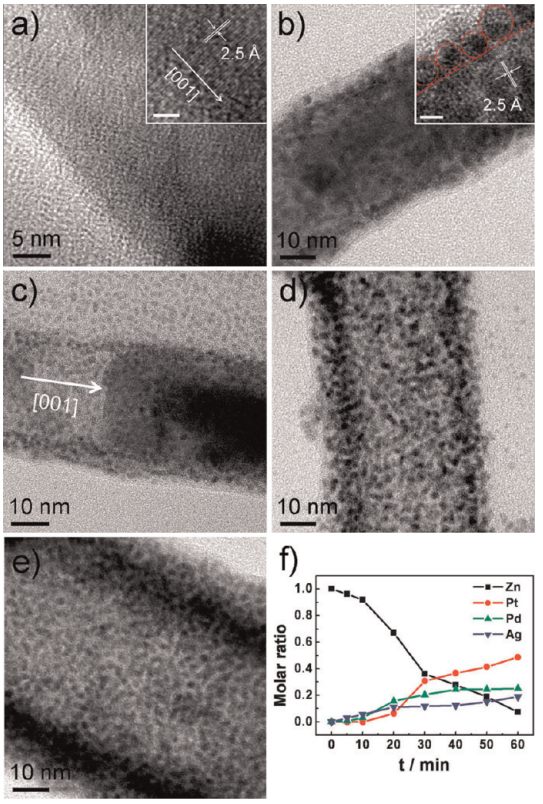

Figure 3. TEM images of Pt−Pd−Ag/ZnO nanostructures collected at different reaction times: (a) 0, (b) 10, (c) 20, (d) 30, and (e) 40 min. HRTEM images are shown in the insets of panels a and b. The scale bars in the insets of panels a and b indicate 2 nm. The red circles in the inset of panel b denote the small nanoparticles grown on the surface of ZnO NW. (f) Changes in the molar ratios of Zn, Pt, Pd, and Ag during the reaction determined by ICP−AES analyses.

surface of the ZnO NW (Figure 3b). The HRTEM image shown in the inset of Figure 3b clearly reveals the presence of ZnO NWs with distinct lattice fringes and several nanoparticles (denoted as red circles). As more nanoparticles were deposited onto the ZnO NW surface to construct the shell, the ZnO NWs started to dissolve along the [001] direction and became shorter, leaving a network of nanoparticles with a tubular structure, as shown in Figure 3c. The dissolution of ZnO could be explained by the reduction mechanism of metal precursors with citrate. The pH of the reaction mixture decreases as the reaction proceeds due to the consumption of OH^- ions through the deprotonation of citrate, which is coordinated to metal precursor, during the reduction of metal precursors with citrate.[17,18,25] In fact, the pH of the reaction mixture was decreased to 3 at the final stage of the process. This results in dissolution of the ZnO NWs, because ZnO can readily be dissolved in an acidic solution.[26,27] The selective dissolution of ZnO NWs along the [001] direction can be ascribed to the faster etching rate of the polar (001) planes, which have high surface energy, relative to that of the nonpolar planes parallel to the *c*-axis.[26] After 30 min of reaction, few ZnO NWs existed and well-defined tubular structures formed

with a denser aggregation of nanoparticles (Figure 3d). The tubular walls became thicker along with the rough outer surface after 40 min (Figure 3e). The formation process of trimetallic NTs was also reflected in the temporal changes of their composition during the reaction measured by ICP–AES analyses (Figure 3f). As the reaction proceeded, the Zn component gradually decreased and the proportions of Pt, Pd, and Ag increased. Elemental mapping of Zn obtained by the HAADF-STEM-EDS on the NT prepared by 1 h of reaction further showed that ZnO NW templates were almost removed after the process (Figure S5 in SI). As shown in Figure 3f, a rapid increase in the Pt content after 30 min of reaction time relative to the other two metals was observed. This may be ascribed to the accelerated reduction of Pt precursors by galvanic replacement reaction between the Pt precursors in solution and the deposited Ag and/or Pd.

Controlled reduction kinetics through a complementary effect between metal precursors and the nucleation sites on the surface of ZnO NWs are thought be the key to the successful formation of multimetallic alloy NTs. This could be verified by several control experiments. First, the intrinsic reduction potential of individual metal precursors was investigated in the absence of ZnO NWs. Either $PtCl_4^{2-}$ or $PdCl_4^{2-}$ was hardly reduced by citrate, whereas Ag^+ was reduced to form 50–100 nm nanoparticles with a range of shapes (Figure S6a in SI). However, Pt and Pd monometallic NTs were generated, respectively, by the reaction with $PtCl_4^{2-}$ and $PdCl_4^{2-}$ precursors in the presence of ZnO NWs (Figure S6b,c in SI). This implies that ZnO NWs provide heterogeneous nucleation sites for metal atoms, facilitating the reduction of metal precursors on the NW surfaces by lowering the activation energy for nucleation. Interestingly, the reduction of Ag^+ in the presence of ZnO NWs did not yield a tubular structure; instead 50–100 nm sized particles were grown (Figure S6d in SI). This indicates that Ag atoms nucleate in solution through homogeneous nucleation rather than on the surface of the ZnO NW *via* heterogeneous nucleation under the present experimental conditions. On the basis of these results of control experiments together with the feasible formation of Ag-containing multimetallic NTs, that is, Pt–Ag, Pd–Ag, and Pt–Pd–Ag NTs, in the presence of multiple metal precursors, it is posited that $PtCl_4^-$ and/or $PdCl_4^-$ retarded the reduction kinetics of Ag^+ and thus prevented homogeneous nucleation, resulting in the formation of multimetallic alloy NTs. In previous studies on the synthesis of multimetallic nanostructures including our studies, it has been found that the presence of multiple metal precursors in the reaction media can modulate the inherent reduction kinetics of constituent metals, thereby influencing the nucleation and growth habit of nanostructures.[28–31] This could be because the interactions of the counterions in solution with the deposited metals and with other metal salts in solution can change the solubility of metals, thus altering their reduction kinetics. These findings verify that the present method is a facile and general strategy for the synthesis of multimetallic alloy NTs, irrespective of the different reduction kinetics of constituent metals.

The present approach could also allow the production of multimetallic alloy NTs with diverse compositions through adjustment of the relative amounts of metal precursors in growth solutions. SEM images and ICP–AES data of the prepared multimetallic NTs with various compositions are presented, respectively, in Figure S7 and Table S1 in SI. Pt–Pd binary alloy NTs with different compositions of Pt and Pd were synthesized by varying the relative amount of each precursor, such as Pt:Pd = 2:1, 1:1, and 1:2 (Figure S7a in SI). On the contrary, in the case of Ag-containing bimetallic NTs, Pt–Ag and Pd–Ag NTs, the relative amount of Ag that can be used in the formation of NTs was somewhat limited: nanoparticles as well as NTs were produced when the molar ratios of Ag to Pt or Pd in the growth solutions exceeded 1 ($Ag/Pt \geq 1$ or $Ag/Pd \geq 1$) (Figure S7b,c in SI). This difference can be ascribed to the greater tendency of the Ag precursors to be reduced homogeneously than the Pt or Pd precursor, as described in the previous section. For Pt–Pd–Ag ternary alloy NTs, we could prepare uniform NTs with a number of compositions by controlling the relative amount of each precursor in the reaction mixture (Figure S7d and Table S1 in SI). These results demonstrate that our method can be used as a general and effective synthetic tool to generate metallic NTs having multiple components with various compositions.

To investigate the catalytic functions of multimetallic alloy NTs, the Pt–Pd binary alloy NTs were selected representatively as an electrocatalyst toward ethanol oxidation. It is well-known that Pd-based nanostructures can be used as efficient electrocatalysts for ethanol oxidation in alkaline media, given the fact that they have some advantages in this media such as enhanced kinetics and reduced corrosion of the materials.[32–35] For electrochemical experiments, Pt–Pd NTs were prepared on an indium–tin oxide (ITO) glass substrate (Figure S8a in SI). For comparison, Pt–Pd dendritic nanoparticles (NPs), monometallic Pd NTs grown on ITO glass, and commercial Pd/C (10 wt %, Aldrich) were also prepared (see Methods section and Figures S8c and S9 in SI). Figure 4a shows cyclic voltammograms (CV) of ethanol oxidation at Pt–Pd NTs, Pt–Pd NPs, Pd NTs, and Pd/C in 0.1 M KOH solution containing 0.5 M ethanol. The current values were normalized to the electrochemically active surface areas (ECSA) estimated by measuring the Coulombic charges for oxygen desorption (Figure S10 in SI). Pt–Pd bimetallic catalysts, Pt–Pd NTs, and

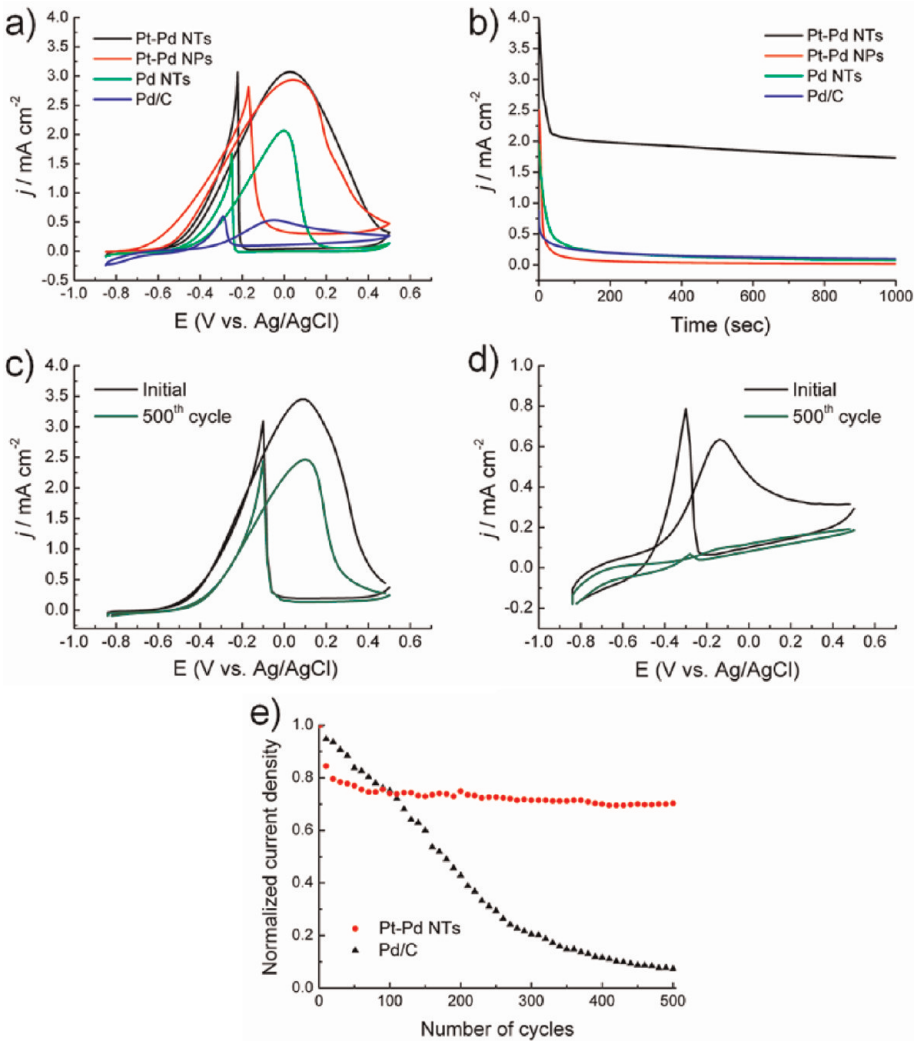

Figure 4. (a) CVs in 0.1 M KOH + 0.5 M ethanol of the Pt−Pd NTs, Pt−Pd NPs, Pd NTs, and Pd/C on ITO electrodes. Scan rate: 50 mV s^{-1}. (b) CA curves for the Pt−Pd NTs, Pt−Pd NPs, Pd NTs, and Pd/C at −0.1 V *vs* Ag/AgCl. CVs in 0.1 M KOH + 0.5 M ethanol of the Pt−Pd NTs (c) and Pd/C (d) before and after durability test. (e) Normalized current densities of the Pt−Pd NTs and Pd/C toward ethanol electro-oxidation as a function of the number of potential cycles.

Pt−Pd NPs exhibited higher current densities compared to monometallic Pd NTs and Pd/C; the maximum current densities on the forward sweep were 3.07, 2.93, 2.06, and 0.533 mA cm^{-2} for the Pt−Pd NTs, Pt−Pd NPs, Pd NTs, and Pd/C, respectively. Furthermore, the Pt−Pd NTs and Pt−Pd NPs showed more negative onset potential values than those of the Pd NTs and Pd/C; −0.616, −0.645, −0.570, and −0.515 V *vs* Ag/AgCl for the Pt−Pd NTs, Pt−Pd NPs, Pd NTs, and Pd/C, respectively. The enhanced electrocatalytic activity of the Pt−Pd bimetallic catalysts could be due to the synergetic effect from the constituent metals. The Pt−Pd alloy has a modified electronic structure compared to its monometallic counterparts, resulting in promotion of the electrocatalytic properties.[36−38] To examine the electronic structure of catalysts, binding energies for Pd 3d of the Pt−Pd and Pd NTs were characterized by X-ray photoelectron spectroscopy (XPS). Binding energies for Pd $3d_{5/2}$ of Pt−Pd and Pd NTs were 337.29 and 337.71 eV, respectively (Figure S11 in SI). The lower binding energy of Pt−Pd NTs than that of the Pd NTs unambiguously indicates the modification of electronic structure by the alloy formation. On the other hand, Pt−Pd and Pd NTs showed higher current densities than their nanoparticulate counterparts. This can be attributed to the high density of active surface sites on NTs caused by both the hollow tubular morphology and the small nanoparticles composing the NTs. Additionally, the anisotropic NT structure and the porous wall can promote mass transport, which improves the catalytic activity.[39,40]

The long-term stability is the key issue for developing efficient electrocatalysts. To evaluate the electrochemical stabilities of the catalysts, chronoamperometric (CA) measurements were performed at −0.1 V *vs* Ag/AgCl in 0.1 M KOH + 0.5 M ethanol (Figure 4b). Noticeably, significantly higher oxidation current was retained on the Pt−Pd NTs compared to those on other

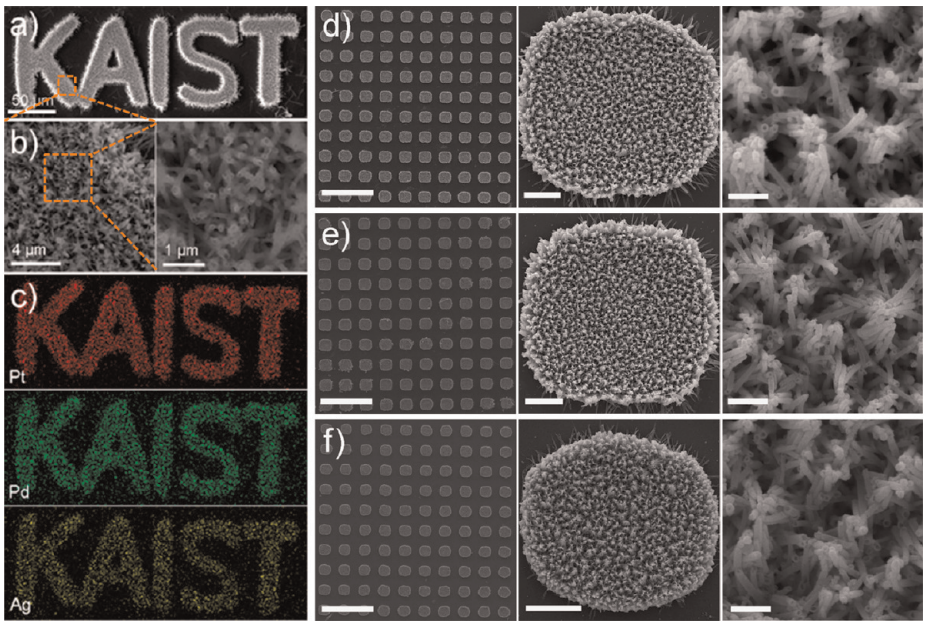

Figure 5. (a) SEM image of letter pattern of Pt−Pd−Ag NTs. (b) High-magnification SEM images of Pt−Pd−Ag NTs. (c) SEM-EDS elemental mapping images of Pt−Pd−Ag NT pattern shown in panel a. (d) SEM images of pristine dot pattern of Pt−Pd−Ag NTs on PI substrate. SEM images of the dot pattern of Pt−Pd−Ag NTs after 10^5 cycles of (e) positive and (f) negative bending and relaxing with a radius of curvature of 4.00 mm. The scale bars in panels d−f indicate 100, 5, and 0.5 μm for the first, second, and third column, respectively.

catalysts after an initial current drop for 50 s. This indicates the prominent electrocatalytic stability of the Pt−Pd NTs. TEM investigations showed that the small segments of the Pt−Pd NTs fell apart from the surface of the NTs after 30 s of CA measurement (Figure S12 in SI). The Pt:Pd molar ratio of the NTs after 30 s of CA measurement was 26:74, which was similar to the initial value. Accordingly, the initial drop in current density of the Pt−Pd NTs can be attributed to the slight disassembly of small segments of NTs. To further examine the stability of the Pt−Pd NTs, accelerated durability tests were also performed, which were carried out in 0.1 M KOH + 0.5 M ethanol solutions by applying cyclic potential sweeps between −0.85 and 0.5 V *vs* Ag/AgCl at a scan rate of 50 mV s^{-1}. As shown in Figure 4c, the Pt−Pd NTs showed a loss of 29.8% in current density after 500 cycles of ethanol oxidation. The plot of normalized current density as a function of cycle number shows that nearly steady current was obtained after 70 cycles (Figure 4e). In contrast, the current density of Pd/C remarkably decreased after a durability test (Figure 4d). The oxidation current on Pd/C declined continuously during the test, and the current loss was as high as about 93% after 500 cycles (Figure 4e). The enhanced durability of the Pt−Pd NT catalysts was further confirmed by the SEM measurements of catalysts after durability test. There is no significant collapse of tubular structures in the Pt−Pd NTs, except a little shrink in dimension (Figure S8b in SI), whereas extensive aggregation and coalescence of particles were observed for the Pd/C after the test (Figure S8d in SI). Considering the fact that deactivation of supported NP electrocatalysts are associated with dissolution, Ostwald ripening, and coalescence of NPs during the electrochemical reaction,[35,41] enhanced durability of the Pt−Pd NTs can be attributed their tubular structure with the interconnected network of small NPs, which is less vulnerable than NPs to the deactivation processes. On the other hand, the comparison of electrocatalytic stability between the bimetallic Pt−Pd and monometallic Pd NTs revealed that the incorporation of Pt in Pd catalysts has a profound effect on their stability.

An appealing feature of the strategy developed in this work is that it can even allow the fabrication of 2D arrays of multimetallic NT on various substrates with precisely controlled patterns. Figure 5a shows a SEM image of the patterned array of Pt−Pd−Ag ternary alloy NTs on Si wafer, which was fabricated by using a patterned ZnO NW array as a template (see Methods section). Enlarged SEM images shown in Figure 5b and SEM-EDS elemental mapping results displayed in Figure 5c reveal the successful formation of Pt−Pd−Ag ternary alloy NTs. Patterned arrays of ternary alloy NTs could also be prepared on the flexible polyimide (PI) substrates (Figure 5d). The fatigue tests for the patterned NT arrays on PI films through 10^5 cycles of bending and relaxing demonstrate that the prepared NT arrays have excellent mechanical robustness and adhesion stability (Figure 5e,f). These types of patterned arrays of multimetallic NT cannot be easily achieved by using conventional techniques, and will

be very beneficial for a number of electronic and sensing applications.

CONCLUSION

Binary and ternary alloy NTs have been synthesized in aqueous solution by using ZnO NWs as sacrificial templates. Nanosized metallic segments formed a network along the surface of the ZnO NWs over the course of reaction, while the ZnO NWs were dissolved concomitantly owing to the decrease of pH induced by the reduction of metal precursors, eventually yielding well-defined multimetallic alloy NTs with porous walls. The prepared Pt–Pd binary alloy NTs exhibited improved electrocatalytic activity and stability over the Pt–Pd NPs, Pd NTs, and Pd/C toward ethanol oxidation due to their characteristic tubular morphology with well-interconnected nanoporous framework and synergism between two constituent metals. Furthermore, our approach can facilitate the fabrication of patterned multimetallic NT arrays on solid and flexible substrates with strong mechanical robustness. The present templating method does not require any extra steps to remove templates or additional surfactants which are often required to control the shape of nanostructures. This strategy offers a convenient, versatile, low-cost, and highly valuable approach to the fabrication of multimetallic nanostructures with various components and compositions, and can be extended to the production of other multidimensional hollow nanostructures by tailoring the morphology of the ZnO template.

METHODS

Chemicals and Materials. Zinc acetate dihydrate ($Zn(CH_3COO)_2 \cdot 2H_2O$, 99.999%), zinc nitrate hexahydrate ($Zn(NO_3)_2 \cdot 6H_2O$, 98%), hexamethylenetetramine (99+%), polyethylenimine (PEI, M_W = 800), K_2PtCl_4 (99.9%), K_2PdCl_4 (98%), $AgNO_3$ (99.0%), and sodium citrate dihydrate (99%) were purchased from Aldrich and used as received. Other chemicals were reagent grade, and Milli-Q water with a resistivity of greater than 18.0 MΩ·cm was used in the preparation of aqueous solutions.

Synthesis of ZnO NW Arrays. ZnO NW arrays on Si wafer or ITO glass substrates were fabricated by following the literature.[42] Prior to the growth of ZnO NW array, the substrate was cleaned by sequentially sonicating in acetone, isopropyl alcohol, ethanol, and deionized water, and then dried in a N_2 gas stream. The substrate was wetted with a droplet of presynthesized ZnO nanoparticle solution in methanol, rinsed with ethanol, and then dried with N_2 gas. This step was repeated several times for the complete coverage of seeds. Then, ZnO NWs were grown hydrothermally by immersing the seeded substrates in aqueous solutions containing zinc nitrate (25 mM), hexamethylenetetramine (25 mM), and PEI (6 mM) at 95 °C for 2.5 h. The substrate was then removed from solution, washed with deionized water, and dried.

Fabrication of Patterned ZnO NW Arrays. To make ZnO NW arrays with dot and letter patterns, photoresist (PR, AZ 9260) spin-coated on Si or PI substrate was patterned by UV photolithography. Then, Cr thin film (thickness = 50 nm) was deposited by thermal evaporation as an adhesion layer, and ZnO thin film was deposited by sputtering at 200 W for 3 min. After the deposition of Cr and ZnO layers, the PR was removed by lift-off process. Then, ZnO NWs were grown using the identical method described in the previous section.

Synthesis of Multimetallic NTs. In a typical synthesis of multimetallic NTs, 2 mL of an aqueous solution of mixed metal precursor (3 mM) was added to an aqueous solution of sodium citrate dihydrate (0.03 mL, 30 mM), and then ZnO NW array grown on substrate was immersed into this growth solution. The reaction mixture was then heated at ~90 °C for about 1 h in a conventional drying oven.

Synthesis of Dendritic Pt–Pd NPs. In a typical synthesis of Pt–Pd NPs, 1 mL of 5 mM aqueous solutions of K_2PtCl_4 and K_2PdCl_4 were added to 46 mL of deionized water and then aqueous solutions of cetyltrimethylammonium bromide (CTAB) (1 mL, 30 mM) and ascorbic acid (1 mL, 100 mM) were added to this solution with vigorous stirring. The resultant mixture was heated to 90 °C. After additional stirring for 5 min, the reaction solution was stored under dark. The resultant hydrosol was centrifuged (10 000 rpm) and redispersed in water three times to remove excess reactants in the solution. The TEM images of the products show that the majority of the sample was dendritic NPs with an average particle size of 22 nm (Figure S8a in SI). The ICP–AES-determined Pt:Pd molar ratio of the prepared Pt–Pd NPs was 46:54.

Characterization. SEM images of the samples were taken with a field-emission scanning electron microscope (FESEM, Phillips model XL30 FEG), and SEM-EDS measurements were performed with a FESEM (FEI, Magellan 400). TEM images and EDS data were obtained with a Phillips Tecnai F20 transmission electron microscope operating at 200 kV after placing a drop of NT dispersion prepared by 10 s sonication. HRTEM and HAADF-STEM characterizations were performed with a Phillips Tecnai G2 F30 Super-Twin transmission electron microscope operating at 300 kV. The effective electron probe size and dwell time used in HAADF-STEM-EDS mapping experiments were 1.5 nm and 200 ms per pixel, respectively. The compositions of products were determined by ICP–AES (Spectro Ciros). XRD patterns were obtained with a Bruker AXS D8 DISCOVER diffractometer using Cu Kα (0.1542 nm) radiation. XPS measurements were carried out with a Thermo MultiLab 2000 using Al Kα X-ray as the light source. CV measurements were carried out in a three-electrode cell using a CH Instrument model 600C potentiostat. NT arrays grown on ITO glasses or drop-casting films of NPs or Pd/C on ITO substrates served as working electrodes. Before CV measurements, the substrates were cleaned again by sequentially washing with acetone, ethanol, and water to remove stabilizing agents on the surface of nanostructures. Pt wire and Ag/AgCl (in saturated KCl) were used as the counter and reference electrodes, respectively. All CVs were obtained at room temperature. The electrolyte solutions were purged with high-purity N_2 gas before use for about 30 min. The fatigue tests for the patterned NT arrays on PI films were performed by following the literature procedure.[43]

Conflict of Interest: The authors declare no competing financial interest.

Acknowledgment. This work was supported by Basic Science Research Programs (2010-0029149), Global Frontier Project (2011-0031870), EPB Center (2008-0062042), and Future-Based Technology Development Program (Nano Fields) (2009-0082640) through the National Research Foundation (NRF) funded by the Korean government (MEST).

Supporting Information Available: Additional experimental data. This material is available free of charge *via* the Internet at http://pubs.acs.org.

REFERENCES AND NOTES

1. Yuan, Q.; Zhou, Z.; Zhuang, J.; Wang, X. Seed Displacement, Epitaxial Synthesis of Rh/Pt Bimetallic Ultrathin Nanowires for Highly Selective Oxidizing Ethanol to CO_2. *Chem. Mater.* **2010**, *22*, 2395–2402.

2. Hong, J. W.; Kim, D.; Lee, Y. W.; Kim, M.; Kang, S. W.; Han, S. W. Atomic-Distribution-Dependent Electrocatalytic Activity of Au–Pd Bimetallic Nanocrystals. *Angew. Chem., Int. Ed.* **2011**, *50*, 8876–8881.
3. Ferrando, R.; Jellineck, J.; Johnston, R. L. Nanoalloys: From Theory to Applications of Alloy Clusters and Nanoparticles. *Chem. Rev.* **2008**, *108*, 845–910.
4. Lu, P.; Dong, J.; Toshima, N. Surface-Enhanced Raman Scattering of a Cu/Pd Alloy Colloid Protected by Poly(*N*-vinyl-2-pyrrolidone). *Langmuir* **1999**, *15*, 7980–7992.
5. Yang, L.-B.; Chen, G.-Y.; Wang, J.; Wang, T.-T.; Li, M.-Q.; Liu, J.-H. Sunlight-Induced Formation of Silver–Gold Bimetallic Nanostructures on DNA Template for Highly Active Surface Enhanced Raman Scattering Substrates and Application in TNT/Tumor Marker Detection. *J. Mater. Chem.* **2009**, *19*, 6849–6856.
6. Greeley, J.; Stephens, L. E.; Bondarenko, A. S.; Johnsson, T. P.; Hansen, H. A.; Jaramillo, T. F.; Rossmeisl, J.; Chorkendorff, I.; Nørskov, J. K. Alloys of Platinum and Early Transition Metals as Oxygen Reduction Electrocatalysts. *Nat. Chem.* **2009**, *1*, 552–556.
7. Adams, B. D.; Wu, G.; Nigro, S.; Chen, A. Facile Synthesis of Pd–Cd Nanostructures with High Capacity for Hydrogen Storage. *J. Am. Chem. Soc.* **2009**, *131*, 6930–6931.
8. Chen, A.; Holt-Hindle, P. Platinum-Based Nanostructured Materials: Synthesis, Properties, and Applications. *Chem. Rev.* **2010**, *110*, 3767–3804.
9. Chen, J.; Lim, B.; Lee, E. P.; Xia, Y. Shape-Controlled Synthesis of Platinum Nanocrystals for Catalytic and Electrocatalytic Applications. *Nano Today* **2009**, *4*, 81–95.
10. Xiong, Y.; Xia, Y. Shape-Controlled Synthesis of Metal Nanostructures: The Case of Palladium. *Adv. Mater.* **2007**, *19*, 3385–3391.
11. Habas, S. E.; Lee, H.; Radmilovic, V.; Somorjai, G. A.; Yang, P. Shaping Binary Metal Nanocrystals through Epitaxial Seeded Growth. *Nat. Mater.* **2007**, *6*, 692–697.
12. Cui, C.-H.; Yu, J.-W.; Li, H.-H.; Gao, M.-R.; Liang, H.-W.; Yu, S.-H. Remarkable Enhancement of Electrocatalytic Activity by Tuning the Interface of Pd–Au Bimetallic Nanoparticle Tubes. *ACS Nano* **2011**, *5*, 4211–4218.
13. Yu, S.; Welp, U.; Hua, L. Z.; Rydh, A.; Kwok, W. K.; Wang, H. H. Fabrication of Palladium Nanotubes and Their Application in Hydrogen Sensing. *Chem. Mater.* **2005**, *17*, 3445–3450.
14. Cui, C.-H.; Li, H.-H.; Yu, J.-W.; Gao, M.-R.; Yu, S.-H. Ternary Heterostructured Nanoparticle Tubes: A Dual Catalyst and Its Synergistic Enhancement Effects for O_2/H_2O_2 Reduction. *Angew. Chem., Int. Ed.* **2010**, *49*, 9149–9152.
15. Chen, Z.; Waje, M.; Li, W.; Yan, Y. Supportless Pt and PtPd Nanotubes as Electrocatalysts for Oxygen Reduction Reaction. *Angew. Chem., Int. Ed.* **2007**, *46*, 4060–4063.
16. Lu, Y.; Chen, W. Nanoneedle-Covered Pd–Ag Nanotubes: High Electrocatalytic Activity for Formic Acid Oxidation. *J. Phys. Chem. C* **2010**, *114*, 21190–21200.
17. Lee, Y. W.; Lim, M. A.; Kang, S. W.; Park, I.; Han, S. W. Facile Synthesis of Noble Metal Nanotubes by Using ZnO Nanowires as Sacrificial Scaffolds and Their Electrocatalytic Properties. *Chem. Commun.* **2011**, *47*, 6299–6301.
18. Lim, M. A.; Lee, Y. W.; Han, S. W.; Park, I. Novel Fabrication Method of Diverse One-Dimensional Pt/ZnO Hybrid Nanostructures and Its Sensor Application. *Nanotechnology* **2011**, *22*, 035601.
19. Bai, F.; Sun, Z.; Wu, H.; Haddad, R. E.; Xiao, X.; Fan, H. Templated Photocatalytic Synthesis of Well-Defined Platinum Hollow Nanostructures with Enhanced Catalytic Performance for Methanol Oxidation. *Nano Lett.* **2011**, *11*, 3759–3762.
20. Sieb, N. R.; Wu, N.-C.; Majidi, E.; Kukreja, R.; Branda, N. R.; Gates, B. D. Hollow Metal Nanorods of Tunable Dimensions and Porosity. *ACS Nano* **2009**, *3*, 1365–1372.
21. Mohl, M.; Kumar, A.; Reddy, A. L. M.; Kukovecz, A.; Komya, Z.; Kiricsi, I.; Vajtai, R.; Ajayan, P. M. Synthesis of Catalytic Porous Metallic Nanorods by Galvanic Exchange Reaction. *J. Phys. Chem. C* **2009**, *114*, 389–393.
22. Huang, M. H.; Mao, S.; Feick, H.; Yan, H.; Wu, Y.; Kind, H.; Weber, E.; Russo, R.; Yang, P. Room-Temperature Ultraviolet Nanowire Nanolasers. *Science* **2001**, *292*, 1897–1899.
23. Lee, J.; Yoon, M. Synthesis of Visible Light-Sensitive ZnO Nanostructures: Subwavelength Waveguides. *J. Phys. Chem. C* **2009**, *113*, 11952–11958.
24. Trejo, M.; Santiago, P.; Sobral, H.; Rendon, L.; Pal, U. Synthesis and Growth Mechanism of One-Dimensional Zn/ZnO Core–Shell Nanostructures in Low-Temperature Hydrothermal Process. *Cryst. Growth Des.* **2009**, *9*, 3024–3030.
25. Ojea-Jiménez, I.; Romero, F. M.; Bastús, N. G.; Puntes, V. Small Gold Nanoparticles Synthesized with Sodium Citrate and Heavy Water: Insights into the Reaction Mechanism. *J. Phys. Chem. C* **2010**, *114*, 1800–1804.
26. She, G.-W.; Zhang, X.-H.; Shi, W.-S.; Fan, X.; Chang, J. C.; Lee, C.-S.; Lee, S.-T.; Liu, C.-H. Controlled Synthesis of Oriented Single-Crystal ZnO Nanotube Arrays on Transparent Conductive Substrates. *Appl. Phys. Lett.* **2008**, *92*, 053111.
27. Liu, J.; Li, Y.; Fan, H.; Zhu, Z.; Jiang, J.; Ding, R.; Hu, Y.; Huang, X. Iron Oxide-Based Nanotube Arrays Derived from Sacrificial Template-Accelerated Hydrolysis: Large-Area Design and Reversible Lithium Storage. *Chem. Mater.* **2010**, *22*, 212–217.
28. DeSantis, C. J.; Peverly, A. A.; Peters, D. G.; Skrabalak, S. E. Octopods *versus* Concave Nanocrystals: Control of Morphology by Manipulating the Kinetics of Seeded Growth *via* Co-Reduction. *Nano Lett.* **2011**, *11*, 2164–2168.
29. Liu, Y.; Walker, A. R. H. Monodisperse Gold–Copper Bimetallic Nanocubes: Facile One-Step Synthesis with Controllable Size and Composition. *Angew. Chem., Int. Ed.* **2010**, *49*, 6781–6785.
30. Lee, Y. W.; Kim, M.; Kang, S. W.; Han, S. W. Polyhedral Bimetallic Alloy Nanocrystals Exclusively Bound by {110} Facets: Au–Pd Rhombic Dodecahedra. *Angew. Chem., Int. Ed.* **2011**, *50*, 3466–3470.
31. Kim, D.; Lee, Y. W.; Lee, S. B.; Han, S. W. Convex Polyhedral Au@Pd Core–Shell Nanocrystals with High-Index Facets. *Angew. Chem., Int. Ed.* **2012**, *51*, 159–163.
32. Ksar, F.; Surencran, G.; Ramos, L.; Keita, B.; Nadjo, L.; Prouzet, E.; Beaunier, P.; Hagege, A.; Audonnet, F.; Remita, H. Palladium Nanowires Synthesized in Hexagomal Mesophases: Application in Ethanol Electrooxidation. *Chem. Mater.* **2009**, *21*, 1612–1617.
33. Tian, N.; Zhou, Z.-Y.; Yu, N.-F.; Wang, L.-Y.; Sun, S.-G. Direct Electrodeposition of Tetrahexahedral Pd Nanocrystals with High-Index Facets and High Catalytic Activity for Ethanol Electrooxidation. *J. Am. Chem. Soc.* **2010**, *132*, 7580–7581.
34. Lee, Y. W.; Kim, M.; Kim, Y.; Kang, S. W.; Lee, J.-H.; Han, S. W. Synthesis and Electrocatalytic Activity of Au–Pd Alloy Nanodendrites for Ethanol Oxidation. *J. Phys. Chem. C* **2010**, *114*, 7689–7693.
35. Guo, S.; Dong, S.; Wang, E. Pt/Pd Bimetallic Nanotubes with Petal-like Surfaces for Enhanced Catalytic Activity and Stability towards Ethanol Electrooxidation. *Energ. Environ. Sci.* **2010**, *3*, 1307–1310.
36. Lim, B.; Jiang, M.; Camargo, P. H. H.; Cho, E. C.; Tao, J.; Lu, X.; Zhu, Y.; Xia, Y. Pd–Pt Bimetallic Nanodendrites with High Activity for Oxygen Reduction. *Science* **2009**, *324*, 1302–1305.
37. Peng, Z.; Yang, H. Synthesis and Oxygen Reduction Electrocatalytic Property of Pt-on-Pd Bimetallic Heteronanostructures. *J. Am. Chem. Soc.* **2009**, *131*, 7542–7543.
38. Yuan, Q.; Zhou, Z.; Zhuang, J.; Wang, X. Pd–Pt Random Alloy Nanocubes with Tunable Compositions and Their Enhanced Electrocatalytic Activities. *Chem. Commun.* **2010**, *46*, 1491–1493.
39. Bi, Y.; Lu, G. Facile Synthesis of Platinum Nanofiber/Nanotube Junction Structures at Room Temperature. *Chem. Mater.* **2008**, *20*, 1224–1226.
40. Lee, K.; Zhang, J.; Wang, H.; Wilkinson, D. P. Progress in the Synthesis of Carbon Nanotube- and Nanofiber-Supported Pt Electrocatalysts for PEM Fuel Cell Catalysis. *J. Appl. Electrochem.* **2006**, *36*, 507–522.
41. Kang, S. W.; Lee, Y. W.; Kim, M.; Hong, J. W.; Han, S. W. One-Pot Synthesis of Carbon-Supported Dendritic Pd–Au

Nanoalloys for Electrocatalytic Ethanol Oxidation. *Chem. Asian J.* **2011**, *6*, 909–913.
42. Greene, L. E.; Law, M.; Goldberger, J.; Kim, F.; Johnson, J. C.; Zhang, Y.; Saykally, R. J.; Yang, P. Low-Temperature Wafer-Scale Production of ZnO Nanowire Arrays. *Angew. Chem., Int. Ed.* **2003**, *42*, 3031–3034.
43. Lim, M. A.; Kim, D. H.; Park, C.-O.; Lee, Y. W.; Han, S. W.; Li, Z.; Williams, R. S.; Park, I. A New Route toward Ultrasensitive, Flexible Chemical Sensors: Metal Nanotubes by Wet-Chemical Synthesis along Sacrificial Nanowire Templates. *ACS Nano* **2012**, *6*, 598–608.